

EFFECTS OF THERMAL BOUNDARY CONDITIONS ON ENTROPY GENERATION DURING NATURAL CONVECTION

Tanmay Basak, Ram Satish Kaluri, and A. R. Balakrishnan

Department of Chemical Engineering, Indian Institute of Technology
Madras, Chennai, India

A comprehensive numerical study on entropy generation during natural convection is studied in a square cavity subjected to a wide variety of thermal boundary conditions. Entropy generation terms involving thermal and velocity gradients are evaluated accurately based on the elemental basis set via the Galerkin finite element method. The thermal and fluid irreversibilities during the conduction and convection dominant regimes are analyzed in detail for various fluids ($Pr = 0.026, 988.24$) within $Ra = 10^3 - 10^5$. Further, the effect of Ra on the total entropy generation and average Bejan number is discussed. It is observed that thermal boundary conditions significantly affect the thermal mixing, temperature uniformity, and the entropy generation in the cavity. A case where the bottom wall is hot isothermal with linearly cooled side walls and adiabatic top wall is found to result in high thermal mixing and a higher degree of temperature uniformity with minimum total entropy generation.

1. INTRODUCTION

The phenomena of natural convection in enclosures continues to be the subject of prime importance in fundamental heat transfer studies as innumerable natural, scientific, and industrial applications are based on the mechanism of natural convection. In contrast to the external flows, the internal buoyancy-driven flows are complex due to essential coupling between the fluid flow and heat transfer. The external flow problems may be simplified assuming that the region outside the boundary layer is unaffected by the boundary layer at a large Rayleigh number. However, such simplification is not possible for confined natural convection flows as the flow field exterior to the boundary layers (core flow) is unknown and that cannot be readily determined from the imposed boundary conditions, as the core flow is in turn dependent on the boundary layers formed at the walls. The problem becomes further complicated when the subregions, such as cells and layers, are embedded in the global core flow.

Thermal boundary conditions play a major role in thermal processing of materials. Although, the conventional heating methodology involving differential heating from the bottom portion is the most common type of boundary condition, various researchers have investigated the effects of alternative thermal boundary conditions

Received 22 October 2010; accepted 29 November 2010.

Address correspondence to A. R. Balakrishnan, Department of Chemical Engineering, Indian Institute of Technology Madras, Chennai 600 036, India. E-mail: arbala@iitm.ac.in

NOMENCLATURE

Be_{av}	average Bejan number	X	dimensionless distance along x coordinate
g	acceleration due to gravity, $m s^{-2}$	y	distance along y coordinate
k	thermal conductivity, $W m^{-1} K^{-1}$	Y	dimensionless distance along y coordinate
l	length of hot/cold section, m	α	thermal diffusivity, $m^2 s^{-1}$
L	side of the square cavity, m	β	volume expansion coefficient, K^{-1}
N	total number of nodes	γ	penalty parameter
p	pressure, Pa	Γ	boundary
P	dimensionless pressure	θ, Θ	dimensionless temperature
Pr	Prandtl number	ν	kinematic viscosity, $m^2 s^{-1}$
R	Residual of weak form	ρ	density, $kg m^{-3}$
Ra	Rayleigh number	Φ	basis functions
RMSD	root-mean square deviation	ψ	streamfunction
S_ψ	entropy generation due to fluid friction	Subscripts	
S_0	entropy generation due to heat transfer	i	residual number
T	temperature of the fluid, K	k	node number
T_h	temperature of discrete heat sources, K	b	bottom wall
T_c	temperature of cold portions of the cavity, K	l	left wall
T_o	bulk temperature, K	r	right wall
u	x component of velocity	1, 3	cold section
U	x component of dimensionless velocity	2	hot section
v	y component of velocity	cup	cup-mixing
V	y component of dimensionless velocity	avg	spatial average
\hat{V}	dimensionless velocity,		
x	distance along x coordinate		

such as sinusoidal heating, discrete heating, etc., for enhanced thermal processing of materials. Sarris et al. [1] investigated natural convection in an enclosure with sinusoidal heating on the upper wall and adiabatic conditions on the bottom and side walls. Further, Sarris et al. [2] have investigated the effect of discrete heating by horizontal heated strips in an industrial glass melting tank. Study of discrete heating for enhanced oxygen dissolution in molten-metal eutectic was reported by Ma et al. [3]. Cheikh et al. [4] studied natural convection in an air-filled square enclosure heated with a constant source from below, and the effects of various thermal boundary conditions at the top and sidewalls were investigated. Bilgen and Yedder [5] performed a numerical study on natural convection in rectangular enclosures with an active vertical wall that is divided equally, and subjected to sinusoidal heating and cooling. Asan and Namli [6] studied laminar natural convection in a pitched roof of triangular cross-section with summer day boundary conditions on the inclined wall. Analysis of uniform and nonuniform heating boundary conditions for natural convection in a square cavity was presented by Basak et al. [7]. Corcione [8] studied natural convection in various configurations of a rectangular enclosure subjected to heating and cooling at various walls. Saha et al. [9] carried out scale analysis of transient natural convection of an inclined flat plate subjected to ramp cooling, and investigated its effects on the boundary layer. Fusegi et al. [10] performed a three-dimensional study of natural convection in a cubical box to examine the specific effects of the horizontal thermal boundary conditions on the flow structure. Recently, Wang et al. [11]

investigated three-dimensional unsteady natural convection in an inclined porous cavity with time oscillatory boundary conditions. Wang and Hameed [12] studied the effect of bidirectional temperature gradients on the mode transition of natural convection inside an inclined rectangular cavity. Ameziani et al. [13] investigated unsteady natural convection in a vertical, open-ended, porous cylinder heated laterally with a sinusoidal time variation of the temperature. Bednarz et al. [14] reported the studies on the transient flow response in a reservoir subjected to periodic heating and cooling at the water surface.

Optimization of thermal systems for high energy-efficiency is crucial amidst the current energy-crisis scenarios. Although advanced optimization approaches such as artificial neural network and genetic algorithms are being developed, those methods fail to present the physical significance of the optimal case. An emerging optimization method, known as entropy generation minimization (EGM) adequately provides the insights into the factors that affect the energy-efficiency. In the EGM method, classical thermodynamics is combined with transport processes into simple models and optimizations are subjected to finite-size and finite-time constraints [15]. The EGM approach is based on the second law of thermodynamics which states that every process is inherently an irreversible process. Hence, some amount of useful or available energy (called *exergy*) is destroyed during the process due to irreversibilities present, leading to the reduction in maximum achievable efficiency. The loss or destruction of available energy due to the irreversibilities can be quantified in terms of entropy generation based on the Guoy-Stodola theorem [15]. In a thermal convection system, the irreversibilities are due to heat transfer and fluid friction. Thus, optimal design of the natural convection system may be identified by applying the criteria of minimum entropy generation. It may be noted that earlier studies reported in the literature are based on total entropy generation evaluated using field variables obtained from analytical solutions. The latest advancement with regard to thermodynamic optimization is to combine the EGM approach with computational fluid dynamics (CFD) to obtain an entropy map over the entire domain, and to precisely locate the zones and magnitude of entropy generation. The entropy map would be very useful to identify the effect of various parameters on entropy generation locally.

Several studies on EGM applied to various physical systems are reported in the literature [16–21]. Magherbi et al. [16] reported the transient entropy generation at the onset of natural convection. Ilis et al. [17] carried out the studies on entropy generation in rectangular cavities with the same area but different aspect ratios. Baytas [18] presented a comprehensive analysis on the influence of Rayleigh number, Bejan number, and inclination angle on the entropy generation for natural convection in an inclined porous cavity. Yang et al. [19] performed the thermal optimization of a stack of printed circuit board using the entropy generation minimization method. Entropy generation for natural convection in Γ -shaped enclosures was reported by Dagtekin et al. [20]. Entropy generation due to conjugate natural convection in an enclosure bounded by two solids walls of different thicknesses placed at side walls was investigated by Varol et al. [21].

To date, only very few studies have been reported on the effect of thermal boundary conditions on entropy generation during natural convection. Although Zahmatkesh [22] studied entropy generation for uniform and sinusoidal heating conditions at the bottom wall of the porous square cavity, a comprehensive analysis of

entropy generation in enclosures subjected to various thermal boundary conditions is yet to appear in the literature. The current study attempts to address this problem from the viewpoint of identifying energy-efficient heating strategies for thermal processing of various materials. Five different thermal boundary conditions are considered based on the heating of various walls of the square cavity. Entropy maps due to heat transfer irreversibility (S_θ) and fluid friction irreversibility (S_ψ) are obtained for material processing applications with representative fluids such as, molten metals ($Pr=0.026$) and olive oil ($Pr=988.24$) within Rayleigh number, $Ra=10^3-10^5$. Further, the relative dominance of S_θ and S_ψ is analyzed in terms of the average Bejan number.

2. MATHEMATICAL FORMULATION AND SIMULATION

2.1. Velocity and Temperature Distributions

The physical domain of the square cavity is shown in Figure 1. The cavity is subjected to five different thermal boundary conditions mentioned below:

- Case 1. The bottom wall is maintained hot isothermal and the side walls are maintained cold isothermal.
- Case 2. The bottom wall is heated sinusoidally and the side walls are maintained cold isothermal.
- Case 3. The bottom wall is maintained hot isothermal and the side walls are cooled linearly.
- Case 4. The bottom wall is heated sinusoidally, the left wall is cooled linearly, and the right wall is maintained cold isothermal.
- Case 5. The bottom and left walls are maintained hot isothermal and the right wall is maintained cold isothermal.

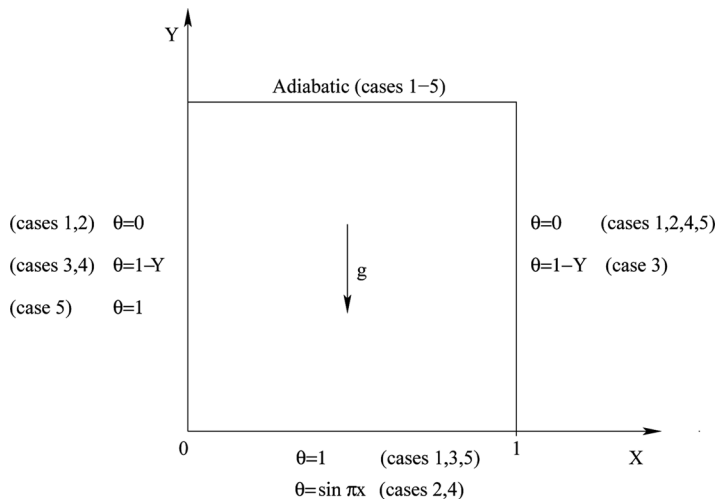


Figure 1. Schematic diagrams of the physical domain. The walls of the cavity are subjected to various thermal boundary conditions, as shown.

The top wall is maintained adiabatic in all cases. It may be noted that the boundary conditions in cases 1–3 are symmetric while those in cases 4 and 5 are asymmetric. The boundary condition in case 1 is commonly found in many food and materials processing applications. Sinusoidal heating (case 2) has applications for the production of float-glass, where one of the walls of the industrial melting tank is heated with a sinusoidal heating profile [1].

The case 3 type of boundary condition occurs in the presence of the hot bottom wall and conducting side walls. During such situations, the bottom portions of the side walls are hotter than the top portion, following a linear temperature profile. The linear heating boundary condition has applications in geology, for example, linearly varying temperature boundary conditions are applied to analyze convection in fractured rocks in the earth's crust as the temperature increases with depth [23]. The case 4 type of boundary conditions are studied in the current work to explore the possibilities of nonuniform heating for efficient thermal processing of materials. A unidirectional flow is expected with boundary conditions similar to those in case 5, and such flow have significance in solidification and crystal growth applications [24].

A two-dimensional laminar flow model is considered. The fluid is assumed to be incompressible and Newtonian with all thermophysical properties except density which is assumed to be constant. Boussinesq approximation is employed for the body force to account the variation of density as a function of temperature and, hence, the temperature field and flow field are coupled. No-slip boundary conditions are assumed at solid boundaries. Under these assumptions, governing equations for steady two-dimensional natural convection flow in the square cavity using conservation of mass, momentum, and energy can be written with the following dimensionless variables or numbers.

$$X = \frac{x}{L}, \quad Y = \frac{y}{L}, \quad U = \frac{uL}{\alpha}, \quad V = \frac{vL}{\alpha}, \quad \theta = \frac{T - T_c}{T_h - T_c},$$

$$P = \frac{\rho L^2}{\rho \alpha^2}, \quad \text{Pr} = \frac{\nu}{\alpha}, \quad \text{Ra} = \frac{g\beta(T_h - T_c)L^3 \text{Pr}}{\nu^2} \quad (1)$$

as

$$\frac{\partial U}{\partial X} + \frac{\partial V}{\partial Y} = 0 \quad (2)$$

$$U \frac{\partial U}{\partial X} + V \frac{\partial U}{\partial Y} = -\frac{\partial P}{\partial X} + \text{Pr} \left(\frac{\partial^2 U}{\partial X^2} + \frac{\partial^2 U}{\partial Y^2} \right) \quad (3)$$

$$U \frac{\partial V}{\partial X} + V \frac{\partial V}{\partial Y} = -\frac{\partial P}{\partial Y} + \text{Pr} \left(\frac{\partial^2 V}{\partial X^2} + \frac{\partial^2 V}{\partial Y^2} \right) + \text{Ra Pr } \theta \quad (4)$$

$$U \frac{\partial \theta}{\partial X} + V \frac{\partial \theta}{\partial Y} = \frac{\partial^2 \theta}{\partial X^2} + \frac{\partial^2 \theta}{\partial Y^2} \quad (5)$$

The boundary conditions for velocities are

$$\begin{aligned} U(X, 0) = U(X, 1) = U(0, Y) = U(1, Y) = 0 \\ V(X, 0) = V(X, 1) = V(0, Y) = V(1, Y) = 0 \end{aligned} \quad (6)$$

and the boundary conditions for temperature in various cases are given below.

Symmetric cases

Case 1

$$\begin{aligned} \theta = 1 & \quad \text{at bottom wall} \\ \theta = 0 & \quad \text{at left and right walls} \\ \frac{\partial \theta}{\partial Y} = 0 & \quad \text{at adiabatic wall} \end{aligned} \quad (7a)$$

Case 2

$$\begin{aligned} \theta = \sin \pi x & \quad \text{at bottom wall} \\ \theta = 0 & \quad \text{at left and right walls} \\ \frac{\partial \theta}{\partial Y} = 0 & \quad \text{at adiabatic wall} \end{aligned} \quad (7b)$$

Case 3

$$\begin{aligned} \theta = 1 & \quad \text{at bottom wall} \\ \theta = 1 - Y & \quad \text{at left and right walls} \\ \frac{\partial \theta}{\partial Y} = 0 & \quad \text{at adiabatic wall} \end{aligned} \quad (7c)$$

Asymmetric cases

Case 4

$$\begin{aligned} \theta = \sin \pi x & \quad \text{at bottom wall} \\ \theta = 1 - Y & \quad \text{at left wall} \\ \theta = 0 & \quad \text{at right wall} \\ \frac{\partial \theta}{\partial Y} = 0 & \quad \text{at adiabatic wall} \end{aligned} \quad (7d)$$

Case 5

$$\begin{aligned} \theta = 1 & \quad \text{at bottom wall} \\ \theta = 1 & \quad \text{at left wall} \\ \theta = 0 & \quad \text{at right wall} \\ \frac{\partial \theta}{\partial Y} = 0 & \quad \text{at adiabatic wall} \end{aligned} \quad (7e)$$

Note, that in Eqs. (1)–(7a–d), X and Y are dimensionless coordinates varying along horizontal and vertical directions, respectively; U and V are dimensionless velocity components in the X and Y directions, respectively; θ is the dimensionless temperature; P is the dimensionless pressure; and Ra and Pr are Rayleigh and Prandtl numbers, respectively.

The momentum and energy balance equations (Eqs. (3)–(5)) are solved using the Galerkin finite element method. The continuity equation (Eq. (2)) has been used as a constraint due to mass conservation and this constraint may be used to obtain the pressure distribution. In order to solve Eqs. (3) and (4), we use the penalty finite element method where the pressure P is eliminated by a penalty parameter γ and the incompressibility criteria given by Eq. (2) which results in,

$$P = -\gamma \left(\frac{\partial U}{\partial X} + \frac{\partial V}{\partial Y} \right) \tag{8}$$

The continuity equation (Eq. (2)) is automatically satisfied for large values of γ . Typical value of γ that yield consistent solutions is 10^7 . Using Eq. (8) the momentum balance equations (Eqs. (3) and (4)) reduce to

$$U \frac{\partial U}{\partial X} + V \frac{\partial U}{\partial Y} = \gamma \frac{\partial}{\partial X} \left(\frac{\partial U}{\partial X} + \frac{\partial V}{\partial Y} \right) + Pr \left(\frac{\partial^2 U}{\partial X^2} + \frac{\partial^2 U}{\partial Y^2} \right) \tag{9}$$

and

$$U \frac{\partial V}{\partial X} + V \frac{\partial V}{\partial Y} = \gamma \frac{\partial}{\partial Y} \left(\frac{\partial U}{\partial X} + \frac{\partial V}{\partial Y} \right) + Pr \left(\frac{\partial^2 V}{\partial X^2} + \frac{\partial^2 V}{\partial Y^2} \right) + Ra \ Pr \ \theta \tag{10}$$

The system of equations (Eqs. (5), (9), and (10)) with boundary conditions (Eq. (6)) is solved by using the Galerkin finite element method [25]. Expanding the velocity components (U, V) and temperature (θ) using basis set $\{\Phi_k\}_{k=1}^N$ as

$$U \approx \sum_{k=1}^N U_k \Phi_k(X, Y) \quad V \approx \sum_{k=1}^N V_k \Phi_k(X, Y) \quad \theta \approx \sum_{k=1}^N \theta_k \Phi_k(X, Y) \tag{11}$$

for

$$0 \leq X, Y \leq 1$$

the Galerkin finite element method yields the following nonlinear residual equations for Eqs. (9), (10), and (5), respectively, at nodes of internal domain Ω .

$$\begin{aligned} R_i^{(1)} = & \sum_{k=1}^N U_k \int_{\Omega} \left[\left(\sum_{k=1}^N U_k \Phi_k \right) \frac{\partial \Phi_k}{\partial X} + \left(\sum_{k=1}^N V_k \Phi_k \right) \frac{\partial \Phi_k}{\partial Y} \right] \Phi_i dX dY \\ & + \gamma \left[\sum_{k=1}^N U_k \int_{\Omega} \frac{\partial \Phi_i}{\partial X} \frac{\partial \Phi_k}{\partial X} dX dY + \sum_{k=1}^N V_k \int_{\Omega} \frac{\partial \Phi_i}{\partial X} \frac{\partial \Phi_k}{\partial Y} dX dY \right] \\ & + Pr \sum_{k=1}^N U_k \int_{\Omega} \left[\frac{\partial \Phi_i}{\partial X} \frac{\partial \Phi_k}{\partial X} + \frac{\partial \Phi_i}{\partial Y} \frac{\partial \Phi_k}{\partial Y} \right] dX dY \end{aligned} \tag{12}$$

$$\begin{aligned}
 R_i^{(2)} = & \sum_{k=1}^N V_k \int_{\Omega} \left[\left(\sum_{k=1}^N U_k \Phi_k \right) \frac{\partial \Phi_k}{\partial X} + \left(\sum_{k=1}^N V_k \Phi_k \right) \frac{\partial \Phi_k}{\partial Y} \right] \Phi_i dX dY \\
 & + \gamma \left[\sum_{k=1}^N U_k \int_{\Omega} \frac{\partial \Phi_i}{\partial Y} \frac{\partial \Phi_k}{\partial X} dX dY + \sum_{k=1}^N V_k \int_{\Omega} \frac{\partial \Phi_i}{\partial Y} \frac{\partial \Phi_k}{\partial Y} dX dY \right] \\
 & + \text{Pr} \sum_{k=1}^N V_k \int_{\Omega} \left[\frac{\partial \Phi_i}{\partial X} \frac{\partial \Phi_k}{\partial X} + \frac{\partial \Phi_i}{\partial Y} \frac{\partial \Phi_k}{\partial Y} \right] dX dY \\
 & - \text{Ra Pr} \int_{\Omega} \left(\sum_{k=1}^N \theta_k \Phi_k \right) \Phi_i dX dY
 \end{aligned} \tag{13}$$

and

$$\begin{aligned}
 R_i^{(3)} = & \sum_{k=1}^N \theta_k \int_{\Omega} \left[\left(\sum_{k=1}^N U_k \Phi_k \right) \frac{\partial \Phi_k}{\partial X} + \left(\sum_{k=1}^N V_k \Phi_k \right) \frac{\partial \Phi_k}{\partial Y} \right] \Phi_i dX dY \\
 & + \sum_{k=1}^N \theta_k \int_{\Omega} \left[\frac{\partial \Phi_i}{\partial X} \frac{\partial \Phi_k}{\partial X} + \frac{\partial \Phi_i}{\partial Y} \frac{\partial \Phi_k}{\partial Y} \right] dX dY
 \end{aligned} \tag{14}$$

Biquadratic basis functions with three point Gaussian quadrature are used to evaluate the integrals in the residual equations except the second term in Eqs. (12) and (13). In Eqs. (12) and (13), the second term containing the penalty parameter (γ) are evaluated with two point Gaussian quadrature (reduced integration penalty formulation [25]). The nonlinear residual equations (Eqs. (12)–(14)) are solved using The Newton-Raphson method to determine the coefficients of the expansions in Eq. (11). The detailed solution procedure is given in an earlier work [7].

2.2. Streamfunction

The fluid motion is displayed using the streamfunction ψ obtained from velocity components U and V . The relationships between streamfunction ψ and velocity components for two-dimensional flows are

$$U = \frac{\partial \psi}{\partial Y} \quad \text{and} \quad V = -\frac{\partial \psi}{\partial X} \tag{15}$$

which yield a single equation

$$\frac{\partial^2 \psi}{\partial X^2} + \frac{\partial^2 \psi}{\partial Y^2} = \frac{\partial U}{\partial Y} - \frac{\partial V}{\partial X} \tag{16}$$

Using the above definition of the streamfunction, the positive sign of ψ denotes anticlockwise circulation, and the clockwise circulation is represented by the negative sign of ψ . Expanding the streamfunction (ψ) using the basis set $\{\Phi\}$ as $\psi = \sum_{k=1}^N \psi_k \Phi_k(X, Y)$ and the relationship for U and V from Eq. (11), the Galerkin

finite element method yields the following linear residual equations for Eq. (16).

$$R_i^s = \sum_{k=1}^N \psi_k \int_{\Omega} \left[\frac{\partial \Phi_i}{\partial X} \frac{\partial \Phi_k}{\partial X} + \frac{\partial \Phi_i}{\partial Y} \frac{\partial \Phi_k}{\partial Y} \right] dX dY - \int_{\Gamma} \Phi_i n \cdot \nabla \psi d\Gamma$$

$$+ \sum_{k=1}^N U_k \int_{\Omega} \Phi_i \frac{\partial \Phi_k}{\partial Y} dX dY - \sum_{k=1}^N V_k \int_{\Omega} \Phi_i \frac{\partial \Phi_k}{\partial X} dX dY \quad (17)$$

The no-slip condition is valid at all boundaries and as there is no cross flow, $\psi = 0$ is used as residual equations at the nodes for the boundaries. The biquadratic basis function is used to evaluate the integrals in Eq. (17), and ψ s are obtained by solving the N linear residual equations (Eq. (17)).

2.3. Entropy Generation

In a natural convection system, the associated irreversibilities are due to heat transfer and fluid friction. According to local thermodynamic equilibrium of the linear transport theory [15], the dimensionless total local entropy generation for a two-dimensional heat and fluid flow in Cartesian coordinates in explicit form is written as

$$S_{\theta} = \left[\left(\frac{\partial \theta}{\partial X} \right)^2 + \left(\frac{\partial \theta}{\partial Y} \right)^2 \right] \quad (18)$$

$$S_{\psi} = \phi \left\{ 2 \left[\left(\frac{\partial U}{\partial X} \right)^2 + \left(\frac{\partial V}{\partial Y} \right)^2 \right] + \left(\frac{\partial U}{\partial Y} + \frac{\partial V}{\partial X} \right)^2 \right\} \quad (19)$$

where S_{θ} and S_{ψ} are local entropy generation due to heat transfer and fluid friction. In the above equation, ϕ , irreversibility distribution ratio is defined as

$$\phi = \frac{\mu T_o}{k} \left(\frac{\alpha}{L \Delta T} \right)^2 \quad (20)$$

In the current study, ϕ is taken as 10^{-4} . A similar value for ϕ was considered by Ilis et al. [17]. A higher value for ϕ was assumed by few earlier researchers [21], and few others have also studied the effect of ϕ on total entropy generation [16, 17, 20]. Note, that ϕ is an adjustable parameter and for a given fluid that varies according to $\Delta T/T_o$, which is termed as the temperature difference number.

Accurate evaluation of derivatives is the key issue for proper estimation of S_{θ} and S_{ψ} . Even a small error in the calculation of temperature and velocity gradients would propagate to a much larger error since the derivatives are powered to 2. As mentioned earlier, the derivatives are evaluated based on the finite element method. The current approach offers special advantage over finite difference or finite volume solutions [20, 21], where derivatives are calculated using some interpolation functions which are avoided in the current work and elemental basis sets (defined by Eq. (11)) are used to estimate S_{θ} and S_{ψ} . The derivative of any function f over an

element e is written as

$$\frac{\partial f^e}{\partial n} = \sum_{k=1}^9 f_k^e \frac{\partial \Phi_k^e}{\partial n} \quad (21)$$

where f_k^e is the value of the function at local node k in the element e . Further, since each node is shared by four elements (in the interior domain) or two elements (along the boundary), the value of the derivative of the function at the global node number (i) is averaged over those shared elements (N^e), i.e.,

$$\frac{\partial f_i}{\partial n} = \frac{1}{N^e} \sum_{e=1}^{N^e} \frac{\partial f_i^e}{\partial n} \quad (22)$$

Therefore, at each node local entropy generation for thermal ($S_{\theta, i}$) and flow fields ($S_{\psi, i}$) are given by

$$S_{\theta, i} = \left[\left(\frac{\partial \theta_i}{\partial X} \right)^2 + \left(\frac{\partial \theta_i}{\partial Y} \right)^2 \right] \quad (23)$$

$$S_{\psi, i} = \phi \left\{ 2 \left[\left(\frac{\partial U_i}{\partial X} \right)^2 + \left(\frac{\partial V_i}{\partial Y} \right)^2 \right] + \left(\frac{\partial U_i}{\partial Y} + \frac{\partial V_i}{\partial X} \right)^2 \right\} \quad (24)$$

Note, that the derivatives $\partial \theta_i / \partial X$, $\partial \theta_i / \partial Y$, $\partial U_i / \partial X$, $\partial U_i / \partial Y$, $\partial V_i / \partial X$, and $\partial V_i / \partial Y$ are evaluated according to Eq. (22). The combined total entropy generation (S_{total}) in the cavity is given by the summation of total entropy generation due to heat transfer ($S_{\theta, \text{total}}$) and fluid friction ($S_{\psi, \text{total}}$), which in turn are obtained via integrating the spatial entropy generation rates (S_{θ} and S_{ψ}) over the domain Ω .

$$S_{\text{total}} = \int_{\Omega} S_{\theta} d\Omega + \int_{\Omega} S_{\psi} d\Omega = S_{\theta, \text{total}} + S_{\psi, \text{total}} \quad (25)$$

where

$$S_{\theta, \text{total}} = \int_{\Omega} \left\{ \left[\frac{\partial}{\partial X} \left(\sum_{k=1}^N \theta_k \Phi_k \right) \right]^2 + \left[\frac{\partial}{\partial Y} \left(\sum_{k=1}^N \theta_k \Phi_k \right) \right]^2 \right\} d\Omega \quad (26)$$

$$S_{\psi, \text{total}} = \phi \int_{\Omega} 2 \left\{ \left[\frac{\partial}{\partial X} \left(\sum_{k=1}^N U_k \Phi_k \right) \right]^2 + \left[\frac{\partial}{\partial Y} \left(\sum_{k=1}^N V_k \Phi_k \right) \right]^2 + \left[\frac{\partial}{\partial Y} \left(\sum_{k=1}^N U_k \Phi_k \right) + \frac{\partial}{\partial X} \left(\sum_{k=1}^N V_k \Phi_k \right) \right]^2 \right\} d\Omega \quad (27)$$

The integrals are evaluated using the three point Gaussian quadrature integration method. The relative dominance of entropy generation due to heat transfer and fluid

friction is given by average Bejan number (Be_{av}), a dimensionless parameter defined as

$$Be_{av} = \frac{S_{\theta, total}}{S_{\theta, total} + S_{\psi, total}} = \frac{S_{\theta, total}}{S_{total}} \quad (28)$$

Therefore, $Be_{av} > 0.5$ implies dominance of heat transfer irreversibility and $Be_{av} < 0.5$ implies dominance of fluid friction irreversibility.

2.4. Cup-Mixing Temperature and RMSD

To compare the thermal mixing in the cavities, the average temperature across the cavity, i.e., cup-mixing temperature, is defined. Cup-mixing temperature is the velocity-weighted average temperature, and is more suitable than spatial average temperature when convective flow exists. The cup-mixing temperature (Θ_{cup}) is given as

$$\Theta_{cup} = \frac{\int \int \widehat{V}(X, Y)\theta(X, Y)dX dY}{\int \int \widehat{V}(X, Y)dX dY} \quad (29)$$

where $\widehat{V}(X, Y) = \sqrt{U^2 + V^2}$. In order to quantify the degree of temperature uniformity in all cases, root-mean square deviation (RMSD) is defined as follows.

$$RMSD = \sqrt{\frac{\sum_{i=1}^N (\theta_i - \Theta_{cup})^2}{N}} \quad (30)$$

It may be noted that lower values of RMSD indicate higher temperature uniformity in the cavity and vice-versa. Also, RMSD cannot exceed 1 as the dimensionless temperature varies between 0 and 1.

3. RESULTS AND DISCUSSION

3.1. Numerical Procedure and Validation

Computations were performed for the domain consisting of 28×28 biquadratic elements, which correspond to 57×57 grid points. An adaptive grid with local refinement along X and Y near the distributed heat sources has been used. Note, that the biquadratic elements with a smaller number of nodes smoothly capture the non-linear variations of the field variables which are in contrast with finite difference/finite volume solutions where a large number of grid nodes are usually required. Detailed computations have been carried out for various fluids of Pr ($Pr = 0.026, 988.24$) within $Ra = 10^3 - 10^5$ for different cases. For discrete heating situations, jump discontinuities exist at the edges of the discrete heat sources which correspond to mathematical singularities. The problem is resolved by specifying the average temperature of the two walls at the hot-cold junctions and keeping the adjacent grid-nodes at the respective wall temperatures [7, 26]. A Gaussian quadrature-based finite element method has been used in the current investigation and this method

provides smooth solutions in the computational domain including the singular points, as *the* evaluation of residuals depends on *the* interior Gauss points.

To assess the accuracy of the present numerical approach, benchmark studies were carried out for the differentially heated square cavity with the hot left wall and cold right wall in the presence of adiabatic top and bottom walls, similar to the case reported by Ilis et al. [17]. They are shown in Figure 2. The results in terms

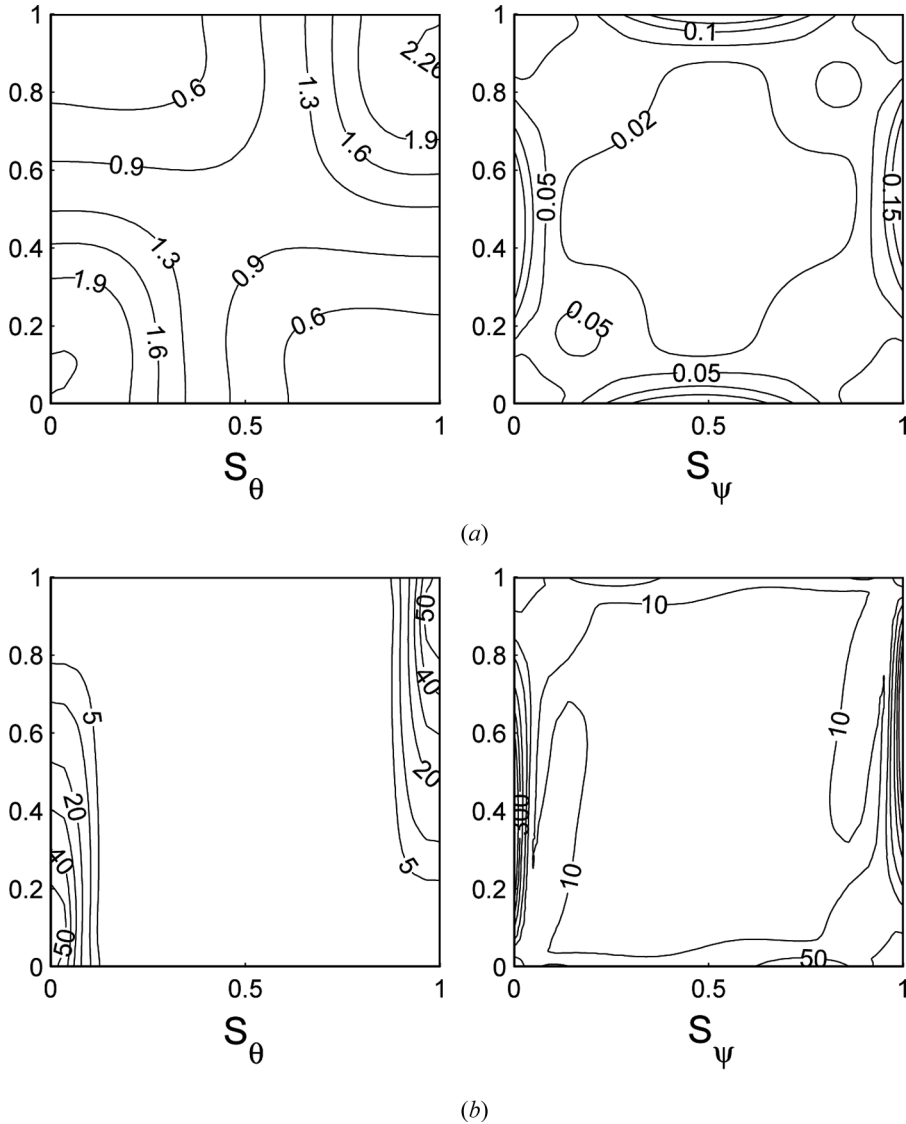


Figure 2. Local entropy generation due to heat transfer ($S_{\theta,i}$) and fluid friction ($S_{\psi,i}$) for a cavity with a hot left wall and cold right wall with adiabatic top and bottom walls at (a) $Ra = 10^3$ and (b) $Ra = 10^5$ for $Pr = 0.7$ (benchmark problem).

of streamlines, isotherms, entropy generation due to heat transfer, and fluid friction are in excellent agreement with the earlier work [17] and the maps of S_θ and S_ψ at $Ra = 10^3$ and 10^5 for $Pr = 0.7$ are shown in Figure 2. Discussion on entropy generation in various cases is presented below.

3.2. Case 1

The boundary conditions for temperature at various walls are given in Eq. (7a). Figure 3 illustrates isotherms (θ), streamlines (ψ), local entropy generation maps due to heat transfer (S_θ), and fluid friction (S_ψ) for $Pr = 0.026$ at $Ra = 10^3$. The bottom wall of the cavity is maintained hot isothermal, the side walls are maintained cold isothermal, and the top wall is adiabatic (see Figure 1a). At low Ra , fluid flow is weak and isotherms are smooth curves, illustrating that heat transfer is primarily

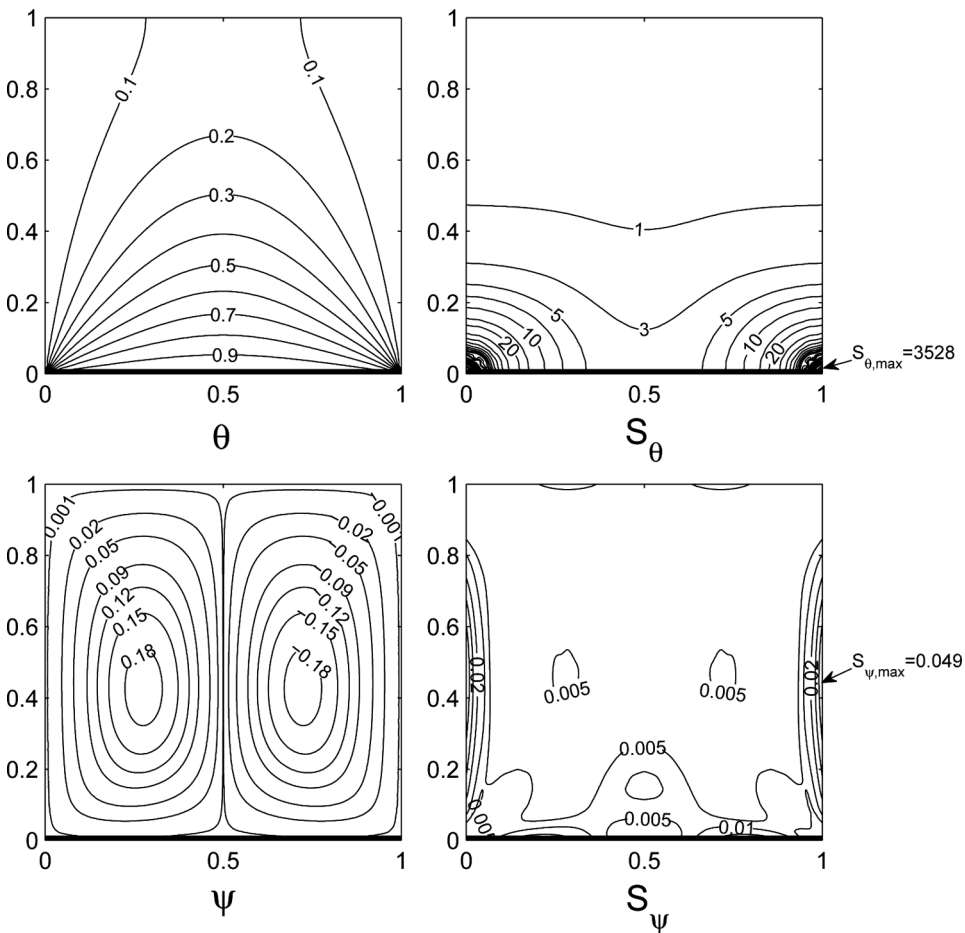


Figure 3. Streamfunction (ψ), temperature (θ), local entropy generation due to heat transfer ($S_{\theta,i}$), and local entropy generation due to fluid friction ($S_{\psi,i}$) contours for case 1 with $Pr = 0.026$ (molten metals) and $Ra = 10^3$.

due to conduction (see Figure 3). A thick thermal boundary layer is observed near the upper portions of side walls with θ varying within 0.1–0.2. The distribution of local entropy due to heat transfer (S_θ) depicts that entropy production is high near the lower corners, where the hot bottom wall is in contact with the cold side walls. The high entropy production is due to high thermal gradients at corner portions. The maximum value of S_θ is found to be 3528, whereas S_θ is almost negligible in the upper portion of the cavity due to low thermal gradients. Entropy generation due to fluid friction is depicted by contours of S_ψ . The values of S_ψ are also found to be small due to weak fluid flow at low Ra.

As Ra increases to 10^5 (Figure 4), the intensity of flow becomes stronger as seen from the magnitudes of streamlines. Multiple cells are induced in the cavity for $Pr = 0.026$. Primary circulation cells occur at the upper portion of the cavity with $|\psi|_{\max} = 6$, while secondary and other tiny circulation cells occur in the lower portion

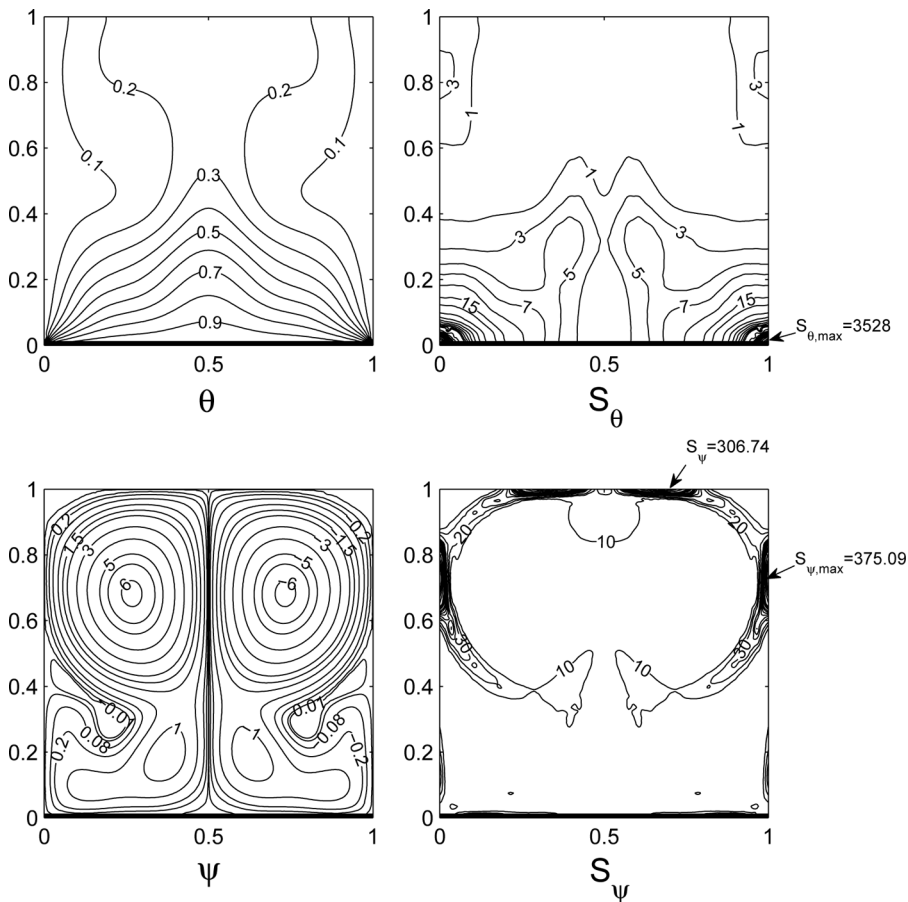


Figure 4. Streamfunction (ψ), temperature (θ), local entropy generation due to heat transfer ($S_{\theta,i}$), and local entropy generation due to fluid friction ($S_{\psi,i}$) contours for case 1 with $Pr = 0.026$ (molten metals) and $Ra = 10^5$.

of the cavity. During enhanced convection, the thermal energy transport from the bottom wall increases significantly as depicted by distorted isotherms. Isotherms with $\theta \geq 0.3$ are observed to be compressed towards bottom wall at higher Ra. Due to high thermal gradient near the bottom wall, dense contours of S_θ occur in that zone and a maxima of S_θ , $S_{\theta,\max} = 3528$ occurs at the bottom corners. Note, that the maxima in S_θ which occurs at the bottom corners remains the same ($=3528$) as in the lower Ra case. On the other hand, smaller entropy generation due to heat transfer is also found to occur at the top corners ($S_\theta \leq 1$) and central regime ($S_\theta = 5$) of the cavity at higher Ra. This is due to contributions of enhanced thermal gradients at those respective portions as a result of enhanced convection.

As the fluid circulation intensifies at high Ra, the large velocity gradients develop in the cavity due to a no-slip boundary condition at the walls. Therefore, a significant amount of exergy is spent for overcoming the fluid friction leading to high entropy generation. The zones of entropy generation due to fluid friction (S_ψ) are depicted by the dense contours near the upper portion of side walls and at the top wall. The maximum S_ψ occurs within $0.6 \leq Y \leq 0.8$ with $S_{\psi,\max} = 375.09$. Note, that significant values of S_ψ also occur in the interior regions of the cavity apart from the wall regions. This is due to the development of high velocity gradients at the interface of two counter-rotating circulations. It is interesting to note that distribution of S_θ occurs mainly in the lower portion of the cavity, while the S_ψ distribution occurs in the upper portion for $Pr = 0.026$ (see Figure 4).

As Pr increases to 988.24, multiple circulations disappear in the cavity and it is observed that the fluid rotates in clockwise and anticlockwise directions in each vertical half of the cavity at $Ra = 10^5$ (Figure 5). Due to high momentum diffusivity of high Pr fluid, intensity of fluid circulation is stronger as seen from $|\psi|_{\max} = 15$. During the convection-dominant mode, compression of isotherms is observed near the bottom wall and near the top portion of side walls. Consequently, large thermal gradients develop along the walls leading to high entropy generation due to heat transfer (S_θ). It may be seen in Figure 5 that the bottom and side walls of the cavity act as stronger active sites for S_θ . The magnitude S_θ is maximum at the top portion compared to the lower portion of the side walls. However, large values of S_θ occur near to the hot bottom wall. The maximum S_θ occurs at the bottom corners with $S_{\theta,\max} = 3528$, similar to that in the $Pr = 0.026$ case. Strong convective flow of high Pr fluid also results in high entropy generation due to fluid friction. It is observed that all walls of the cavity, including the top wall, act as strong active sites for S_ψ . It is found that S_ψ is high along the side walls with $S_{\psi,\max} = 586.57$. Also, a local maxima of S_ψ is found to occur at the central portion of the bottom wall ($S_\psi = 285.24$), while another local maxima in the cavity occurs near the upper corners along the top wall ($S_\psi = 74.48$). It is interesting to note that high entropy generation due to fluid friction also occurs along the vertical center-line, as illustrated by the contours of S_ψ with $S_{\psi,\max} = 200$. This is due to high velocity gradients at the interface of counter-rotating circulation cells. It is also found that the fluid streams from each of the vertical halves converge near the central zone of the bottom wall. A small magnitude of S_ψ is also found to occur at lower corner regimes, where the high velocity fluid changes its direction orthogonally upon reaching the bottom wall. Overall, a large amount of entropy generation due to heat transfer and fluid friction is observed in the cavity for $Pr = 988.24$ compared to that in the $Pr = 0.026$ case.

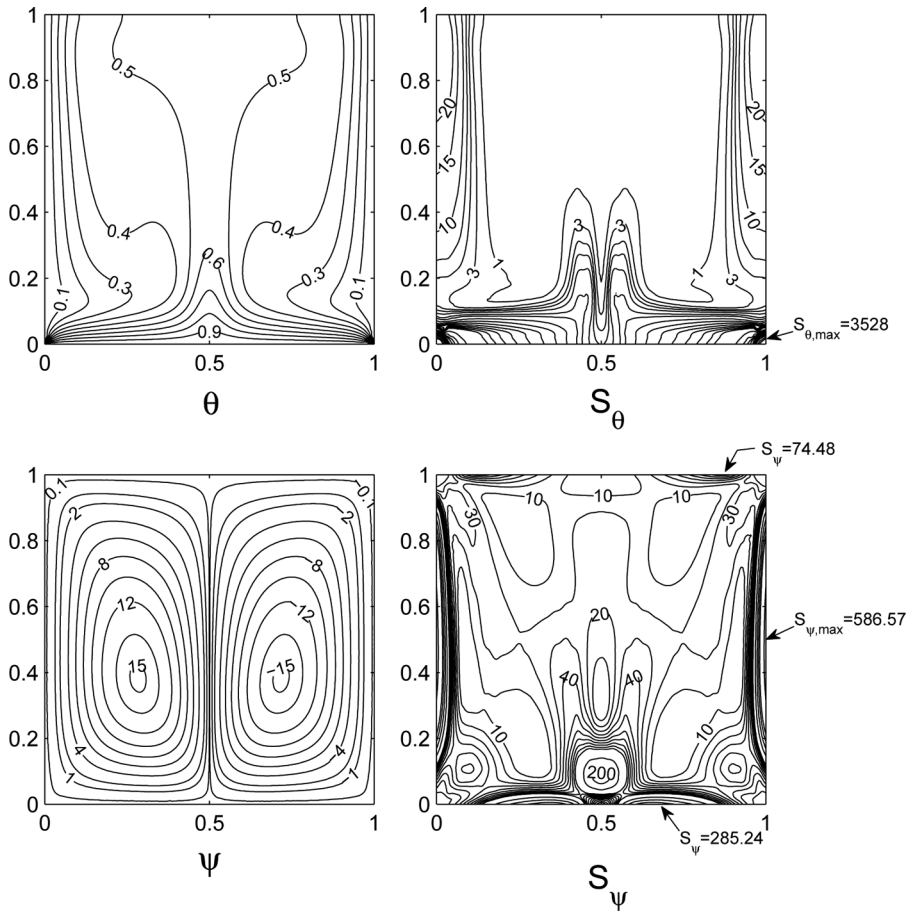


Figure 5. Streamfunction (ψ), temperature (θ), local entropy generation due to heat transfer ($S_{\theta,i}$), and local entropy generation due to fluid friction ($S_{\psi,i}$) contours for case 1 with $Pr=988.24$ (olive oil) and $Ra=10^5$.

It may be observed from Figures 3–5, that the entropy generation due to heat transfer is very high near the lower corner regimes ($S_{\theta,max}=3528$). As mentioned earlier, that is due to high thermal gradients at corner portions as the hot bottom wall is in direct contact with the cold side walls. The singularity problem is circumvented by applying a sinusoidal heating of the bottom wall. A detailed analysis on the effects of the nonuniform sinusoidal heating case for entropy generation due to heat transfer and fluid friction is presented in the following section.

3.3. Case 2

The bottom wall of the cavity is sinusoidally heated according to the Dirichlet boundary condition given in Eq. (7b). Detailed results are not shown for low Ra with $Pr=0.026$, as the distributions are qualitatively similar to those as seen in case 1 with

identical parameters. Symmetric circulation cells with low magnitude of streamlines were observed at low $Ra (=10^3)$ with $Pr=0.026$, similar to that in case 1 (see Figure 3). A smooth distribution of isotherms was observed in the cavity as finite discontinuity would disappear for this case with the given Dirichlet boundary conditions. The maximum value of $|\psi|$ ($|\psi|_{\max}$) was found to be 0.17 indicating weak flow and therefore corresponding heat flow from the bottom wall was also found to be small, resulting in large thermal boundary layer thickness in the upper portion of the cavity. It was observed that the contours of S_θ in the lower portion of the cavity were nearly straight lines and parallel to the bottom wall. As a result of sinusoidal heating, $S_{\theta,\max}$ was found to be only 10.21 which is significantly less compared to that in the uniform heating case (case 1) at identical Ra and Pr . Entropy generation due to fluid friction (S_ψ) was also found to be small for the nonuniform heating case.

At $Ra = 10^5$, the fluid circulations are qualitatively similar to that of the uniform heating case (case 1) for $Pr=0.026$ (see Figures 4 and 6) and the magnitudes

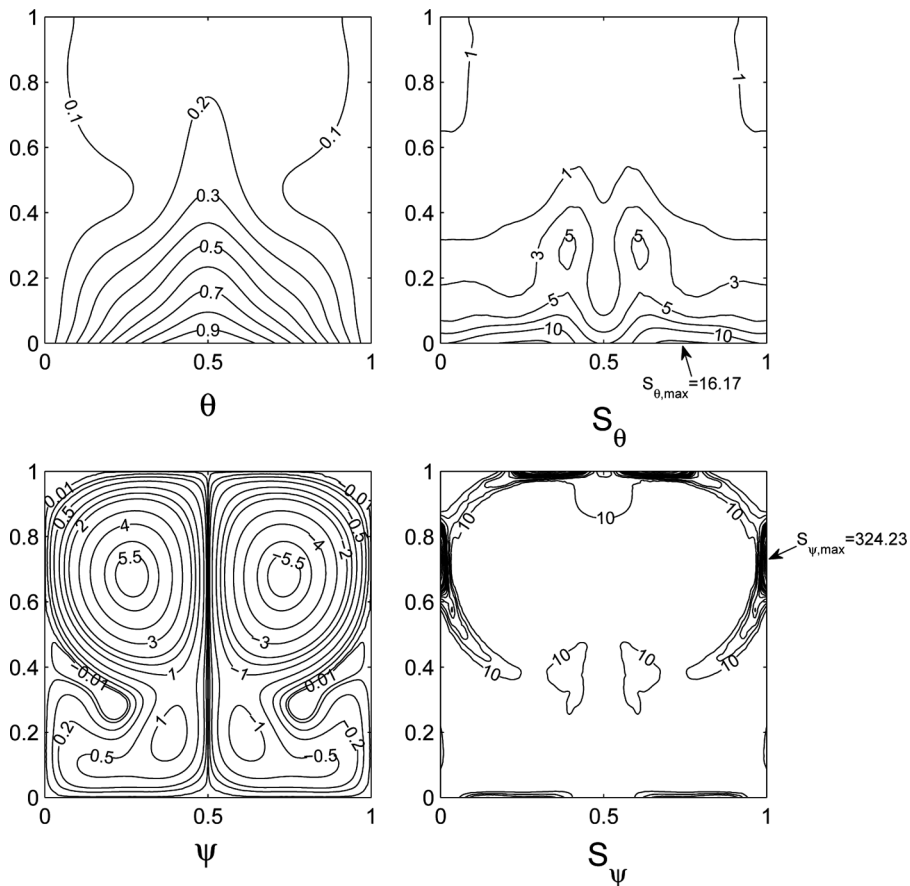


Figure 6. Streamfunction (ψ), temperature (θ), local entropy generation due to heat transfer ($S_{\theta,i}$), and local entropy generation due to fluid friction ($S_{\psi,i}$) contours for case 2 with $Pr=0.026$ (molten metals) and $Ra=10^5$.

of streamlines are found to be slightly lower ($|\psi|_{\max} = 5.5$). The thermal gradients are maximum in the lower portion of the cavity and least at the top central core. Hence, entropy generation due to heat transfer is significant in the lower portion. The compression of isotherm, $\theta = 0.1$, leads to $S_{\theta} = 1$ in the top portion of the side walls. Note, that the change in $S_{\theta, \max} (=16.17)$ is small, even at higher Ra compared to that at $Ra = 10^3$. It may be noted that $S_{\theta, \max}$ in sinusoidal heating cases is much smaller compared to that in the uniform heating case (case 1). The distribution of entropy generation due to fluid friction (S_{ψ}) is similar to that in case 1 at higher Ra as the fluid flow is similar in both the cases as mentioned above. However, the maximum value of S_{ψ} is found to be small with $S_{\psi, \max} = 324.23$, occurring at the top portion of the side wall. Note, that small magnitudes of S_{ψ} are also seen along the bottom wall at higher Ra. As Pr increases to 988.24 (Figure 7), the streamlines and isotherms are qualitatively similar to that in case 1 at identical Ra and Pr. However, the $|\psi|_{\max}$

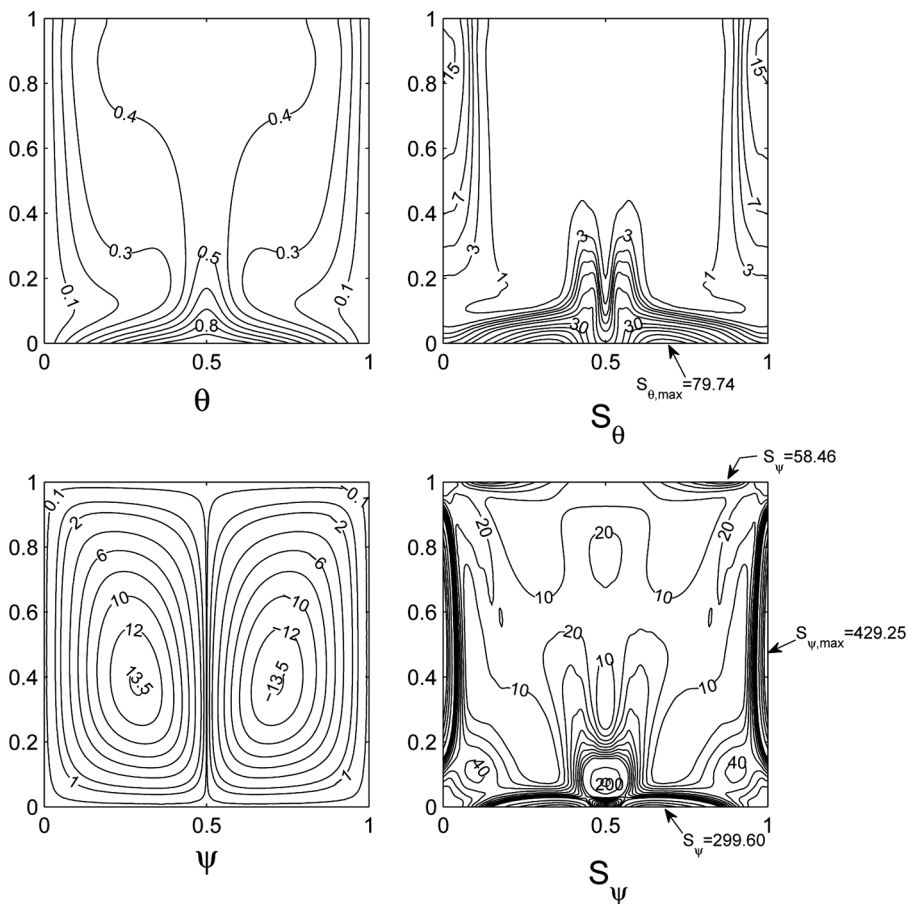


Figure 7. Streamfunction (ψ), temperature (θ), local entropy generation due to heat transfer ($S_{\theta,i}$), and local entropy generation due to fluid friction ($S_{\psi,i}$) contours for case 2 with $Pr = 988.24$ (olive oil) and $Ra = 10^5$.

is observed to be smaller ($=13.5$) and a large region of the cavity is maintained within $\theta=0.3-0.5$. The distribution of S_θ and S_ψ in the cavity are also similar to that in case 1. It may be noted that the lower thermal irreversibility along the bottom wall is due to lower thermal gradients. The value of $S_{\theta,\max}$ is reduced to 79.74. On the other hand, the frictional irreversibility is also lower for sinusoidal heating compared to that in the uniform heating case as seen from the lower value of $S_{\psi,\max}$ ($=429.25$) due to lower magnitudes of $|\psi|$. Note, that the local maxima of S_ψ on the bottom wall is slightly higher in case 2 compared to that in case 1 (see Figures 5 and 7).

3.4. Case 3

In this case, the bottom wall is heated uniformly, whereas the side walls are cooled linearly with a maximum temperature at the bottom portions of side walls and least at the upper portions (Eq. (7c)). It may be noted that the rate of heat input is higher in this case compared to that in cases 1 or 2. Note that the singularity does not occur in this case at the lower corners and thus the isotherms were observed to be nearly horizontal lines up to $\theta=0.5$ as the side and bottom walls are maintained hot (figure not shown). The distributions for $\text{Pr}=0.026$ at $\text{Ra}=10^3$ indicated that the fluid flows in two symmetrical rolls with the eye of the vortex occurring in the upper region of the cavity. The entropy generation due to heat transfer was found to be confined to the top corners with $S_\theta=12.6$. The magnitude of fluid friction irreversibility was also found to be smaller, and a large region of the cavity was maintained as entropy-free region at lower Ra.

As Ra increases to 10^5 (Figure 8), the buoyancy forces become strong and the heat transfer is dominated by convection for $\text{Pr}=0.026$. It is interesting to observe that the fluid flows in four symmetric circulation cells along with tiny circulations at the central region of the side walls and at the lower corners. The lower portion of the cavity is maintained at $\theta \geq 0.6$, while a large upper central region is maintained within $\theta=0.4-0.6$. The entropy generation due to heat transfer is significantly low even during convection-dominant regime as seen from the distributions of S_θ . The maximum value of S_θ ($S_{\theta,\max}$) is found to be only 24. The thermal gradients on the bottom wall occur only at the central regime where $S_\theta=1-7$ is observed. The frictional irreversibility is also found to be remarkably lower, as seen from the contours of S_ψ . Note that in contrast to the previous cases, S_ψ also occurs in the lower region of the cavity and the bottom wall also acts as an active site for S_ψ with local maxima of 182.37 on the bottom wall. The global maxima of S_ψ occurs at the top wall with a $S_{\psi,\max}=189.57$, which is about 49.46% and 41.53% less compared to that in cases 1 and 2, respectively (see Figures 4 and 6).

Thermal and frictional irreversibility maps for $\text{Pr}=988.24$ are illustrated in Figure 9. The flow of higher Pr fluid occurs in symmetrical rolls along with secondary circulations which occur in the lower corners, in contrast to that in the lower Pr case. The stronger fluid circulation with $|\psi|_{\max}=11$ leads to uniform temperature distribution with $\theta=0.6-0.7$ in the upper central region of the cavity. The thermal gradients are found to be high in the upper portions of the side walls and thus, the large entropy generation due to heat transfer irreversibility is observed at that zone with $S_{\theta,\max}=70.48$. Note, that the S_θ near the bottom wall is much lower than

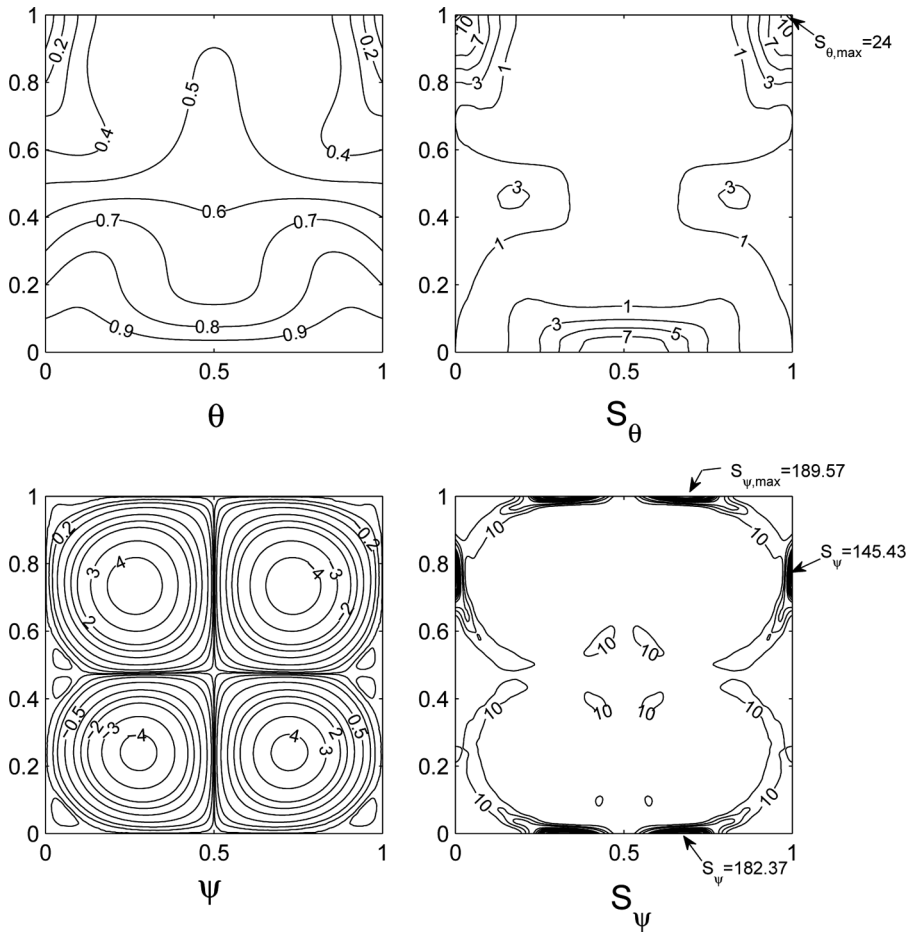


Figure 8. Streamfunction (ψ), temperature (θ), local entropy generation due to heat transfer ($S_{\theta,i}$), and local entropy generation due to fluid friction ($S_{\psi,i}$) contours for case 3 with $Pr = 0.026$ (molten metals) and $Ra = 10^5$.

that at the side walls. The top portions of the side walls also act as strong active sites for entropy generation due to fluid friction with $S_{\psi,max} = 348.02$. The dense contours of S_{ψ} also occur near the edges of the top wall with a local maxima of $S_{\psi} = 93.93$. It is interesting to note that the frictional irreversibility along the bottom wall is small with a local maxima of $S_{\psi} = 56.42$ compared to that in cases 1 and 2, despite the fact the bottom wall is maintained hot in all three cases (see Figures 5, 7, and 9). The entropy generation near the central region of the bottom wall, where the fluid streams converge and flow upwards, is also reduced significantly with local $S_{\psi,max} = 60$ in contrast to $S_{\psi,max} = 200$ in cases 1 and 2 for only a small reduction in $|\psi|_{max}$. Overall, the local distributions of S_{θ} and S_{ψ} for higher and lower limits of Pr are found to be smaller in this case. A comparison of total entropy generation for all cases will be discussed later.

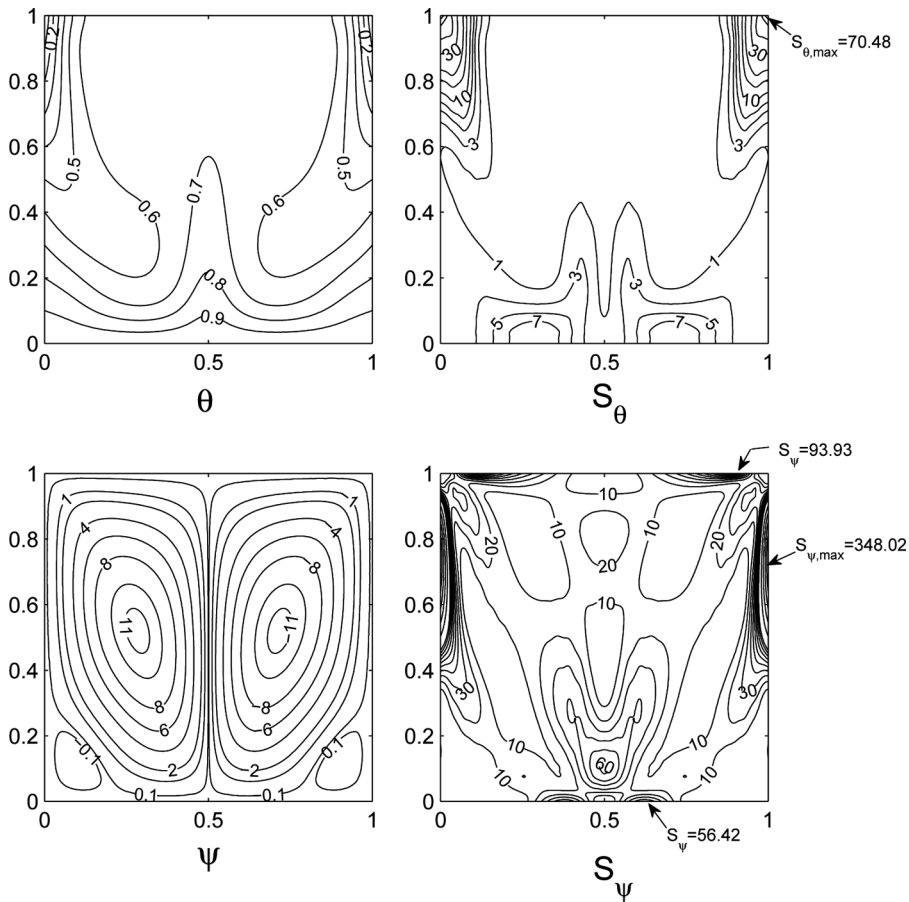


Figure 9. Streamfunction (ψ), temperature (θ), local entropy generation due to heat transfer ($S_{\theta,i}$), and local entropy generation due to fluid friction ($S_{\psi,i}$) contours for case 3 with $Pr=988.24$ (olive oil) and $Ra=10^5$.

3.5. Case 4

The thermal boundary conditions in this case are such that the sinusoidal heating is applied at the bottom wall (see Eq. (7d)). The left side wall wall is heated linearly, whereas the right side wall is maintained cold isothermal. Note, that singularity exists in this case at the lower left corner but that does not occur at the lower right corner. It is interesting to note that the fluid flows unidirectionally in a clockwise direction with a tiny recirculation near the top left corner for $Ra=10^3$ and $Pr=0.026$ (Figure 10). The intensity of the flow at low Ra is higher in this case ($|\psi|_{\max}=0.6$) compared to previous cases at identical Ra and Pr . High thermal gradients are confined to the lower left corner. Consequently, the entropy generation due to heat transfer is largely concentrated to a small region in the lower left corner with $S_{\theta,\max}=3190.72$, whereas only a small magnitude of S_{θ} is observed near the lower portion of the right side wall. The magnitudes of S_{ψ} are also found to be low due to weak fluid flow.

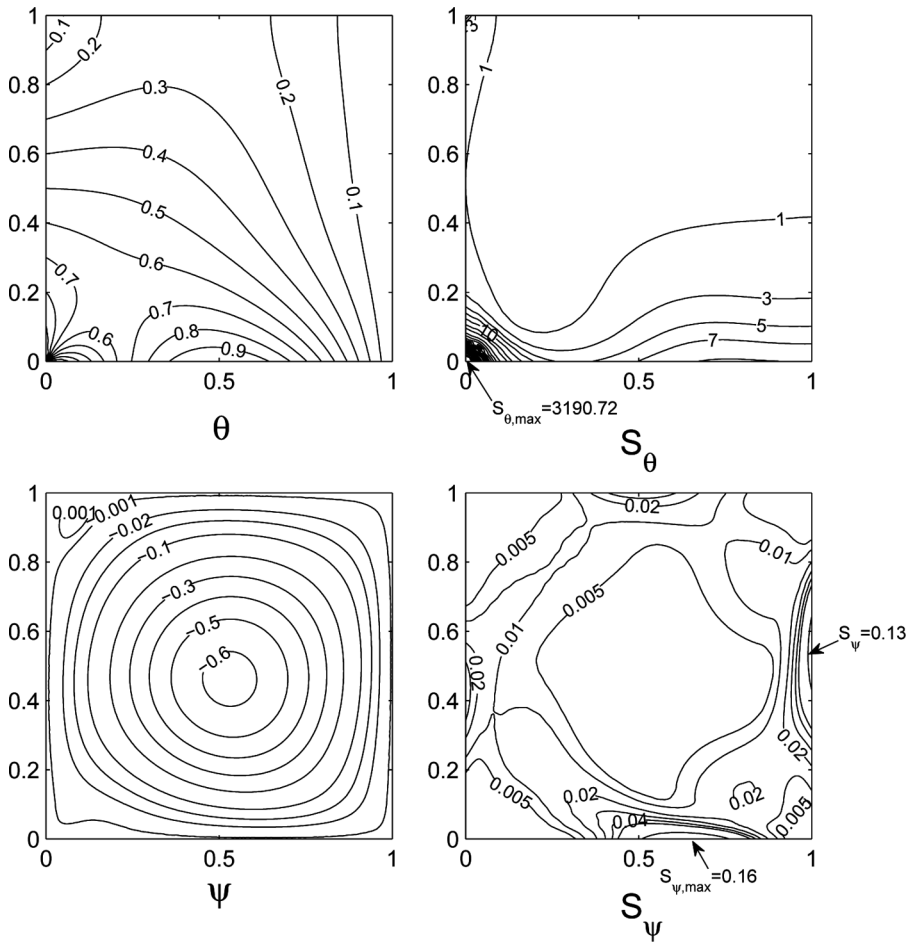


Figure 10. Streamfunction (ψ), temperature (θ), local entropy generation due to heat transfer ($S_{\theta,i}$), and local entropy generation due to fluid friction ($S_{\psi,i}$) contours for case 4 with $Pr = 0.026$ (molten metals) and $Ra = 10^3$.

The unidirectional flow is intensified at higher Ra ($=10^5$) and smaller circulation cells are observed at corners of the cavity (see Figure 11). The thermal mixing in the cavity is significantly enhanced in the cavity, as seen from a uniform temperature distribution varying within $\theta = 0.4-0.5$ at the central core region. The isotherms are compressed towards the bottom and right walls resulting in higher thermal gradients. The entropy generation near the bottom wall is large as seen from the dense contours compared to that on the right wall. The global maxima of S_{θ} remains the same as that in the lower Ra case and the local maxima on the bottom wall is found to be $S_{\theta} = 83.2$. The entropy generation due to fluid friction irreversibility is confined to a circular band with local maxima at the central regions of all the walls. The entropy generation is higher during the downward flow of the fluid along the right and bottom walls with $S_{\theta,max} = 703.72$ and 642.81 , respectively. However, frictional

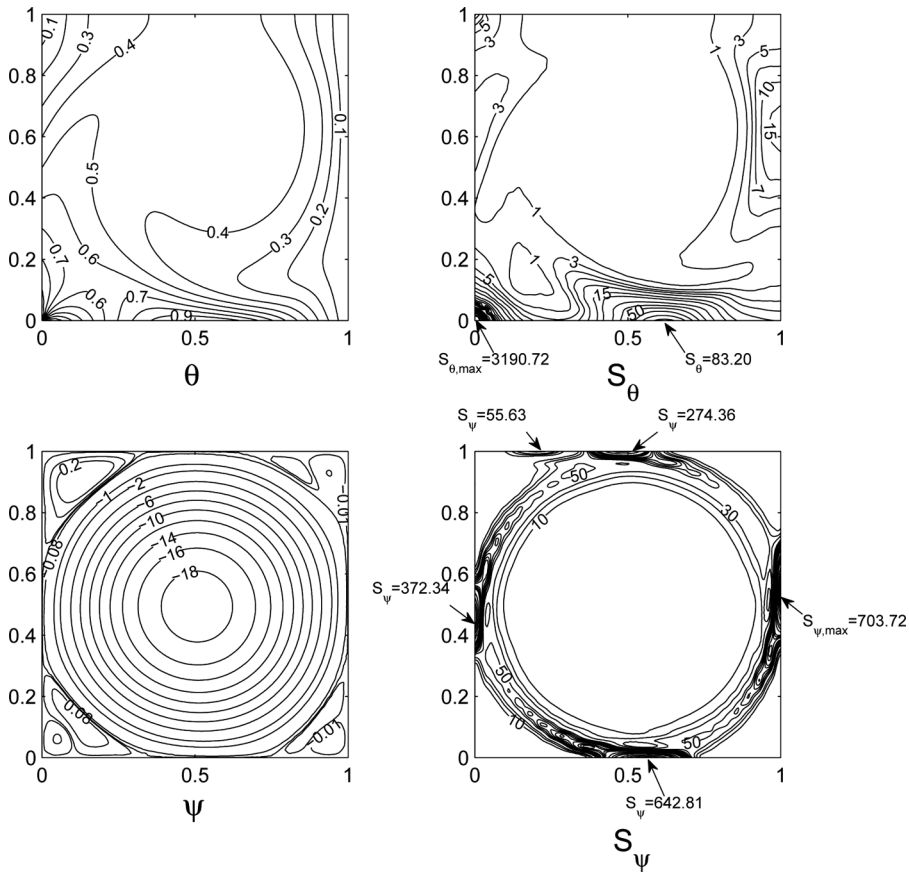


Figure 11. Streamfunction (ψ), temperature (θ), local entropy generation due to heat transfer ($S_{\theta,i}$), and local entropy generation due to fluid friction ($S_{\psi,i}$) contours for case 4 with $Pr=0.026$ (molten metals) and $Ra=10^5$.

irreversibility is found to be lesser during the upward flow along the left and top walls, where the local maxima of S_{ψ} are observed to be 372.34 and 274.36, respectively.

As Pr increases to 988.24 (Figure 12), a large primary circulation cell with $|\psi|_{\max}=16$ and a secondary circulation with $|\psi|_{\max}=2$ is seen at the top left corner. The thickness of the boundary layer along the right wall is further reduced with an increase in Pr , but relatively low thermal gradients are found on the bottom wall. Hence, the local maxima of S_{θ} is found to be 66.10, in contrast to 83.20 in the $Pr=0.026$ case. The entire side wall and majority of the bottom wall contribute significantly to S_{θ} based on dense contours. The right, bottom, and lower portion of the left wall and right edge of the top wall act as active sites for entropy generation due to fluid friction, which is due to the velocity gradients induced by the primary circulation. The maximum value of S_{ψ} occurs on the right wall with a magnitude of 564.74. It is interesting to note that the entropy generation is also induced by change

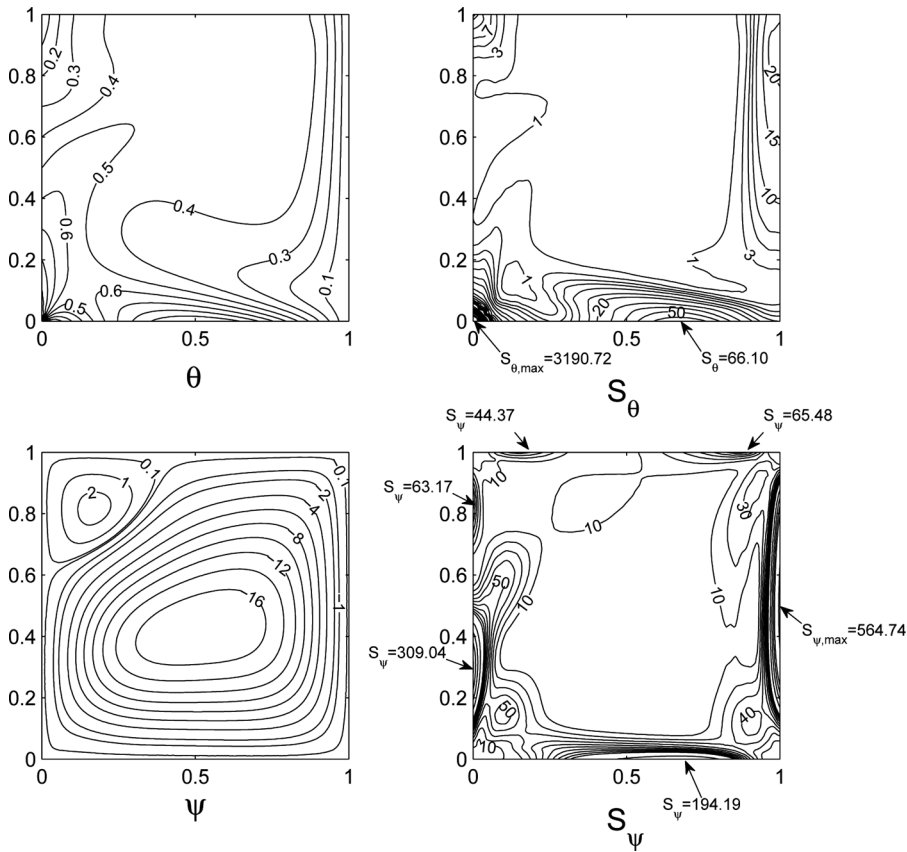


Figure 12. Streamfunction (ψ), temperature (θ), local entropy generation due to heat transfer ($S_{\theta,i}$), and local entropy generation due to fluid friction ($S_{\psi,i}$) contours for case 4 with $Pr = 988.24$ (olive oil) and $Ra = 10^5$.

in flow direction near the lower right corner, where $S_{\psi} = 40$ is observed. However, a higher value of S_{ψ} ($=50$) is observed at the lower left corner. A small magnitude of entropy generation at the top left corner caused by secondary circulation is also observed.

3.6. Case 5

In this case, the bottom and left walls are heated isothermally and the right wall is maintained isothermally cooled (see Eq. (7e)). Note, that singularity occurs at the right corner of the bottom wall. At low Ra , the flow was found to be unidirectional for $Pr = 0.026$, similar to that in Figure 10, and a thick thermal boundary layer spanning almost the entire cavity was observed (figure not shown). The heat transfer irreversibility was found to be confined to a small portion at the lower corner with $S_{\theta,max} = 3528$. The frictional irreversibility was also found to be similar to that in

the previous case (case 4) at low Ra , except that the magnitudes of S_ψ were higher as the fluid flow is relatively stronger due to a higher rate of heat input in this case.

The distribution of θ , ψ , S_θ , and S_ψ at $Ra = 10^5$ and $Pr = 0.026$ illustrated that the fluid flow is similar to that in case 4 at identical Ra and Pr (figure not shown). It was interesting to note that the intensity of the fluid flow was small compared to that in case 4, as $|\psi|_{\max}$ was found to be only 14 in spite of a higher rate of heat input. However, the temperature at the central core was observed to be high with $\theta = 0.6\text{--}0.8$. Entropy generation due to heat transfer was found to be significant along the right wall and right portion of the bottom wall. The entropy generation due to fluid friction was observed to be qualitatively similar to that in case 4 (see Figure 11), but interestingly the contours of S_ψ were observed to be dense, indicating higher magnitudes entropy generation despite a lower value of $|\psi|_{\max}$. The $S_{\psi,\max}$ was found to be 1042.07, which was about 48.08% higher compared to that in case 4.

As Pr increases to 988.24 (Figure 13), the fluid flows as one single cell which spans the entire cavity without any secondary circulations. The fluid flow is stronger

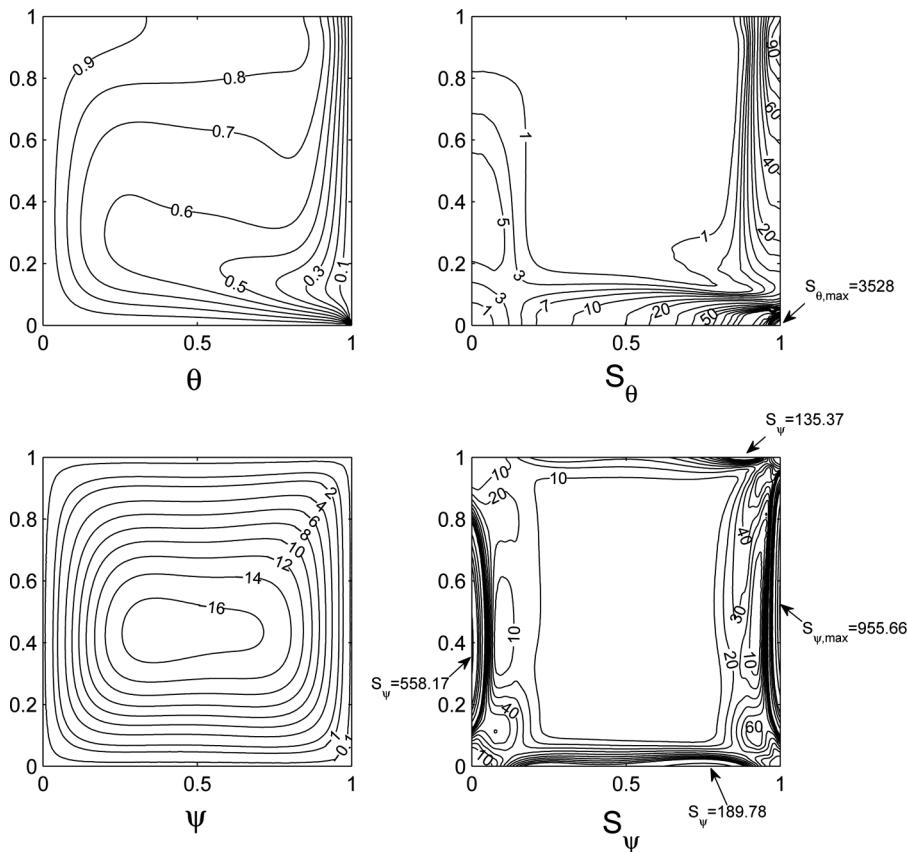


Figure 13. Streamfunction (ψ), temperature (θ), local entropy generation due to heat transfer ($S_{\theta,i}$), and local entropy generation due to fluid friction ($S_{\psi,i}$) contours for case 5 with $Pr = 988.24$ (olive oil) and $Ra = 10^5$.

for the higher Pr case with $|\psi|_{\max} = 16$ during the convection-dominant mode at higher Ra, and hence the thickness of boundary layer is thinner at the right and bottom walls. The bottom wall and the cold right wall act as strong active sites for S_θ . The entropy generation due to heat transfer near the left wall is negligible compared to that on the bottom and right walls. However, the left wall acts as a strong active site for entropy generation due to fluid friction. The friction irreversibility on the left wall is higher than that on the bottom wall as, seen from the local maxima of S_ψ (=558.17) and that is nearly three times the value on the bottom wall. The local maxima on the top wall is 135.37, and the global maxima of S_ψ is observed along the cold right wall with $S_{\psi,\max} = 955.66$.

It is interesting to compare the fluid irreversibility in cases 4 and 5 for Pr = 988.24 at Ra = 10^5 (see Figures 12 and 13). The strength of the primary circulation is same ($|\psi|_{\max} = 16$), but the frictional irreversibility is higher in case 5 as seen from the contours of S_ψ . Note, that $S_{\psi,\max}$ is higher in case 5 (=955.66), but that is only 564.74 on the right wall in case 4.

3.7. Total Entropy Generation, Average Bejan Number, Cup-Mixing Temperature, and Temperature Uniformity

The variation of total entropy generation due to heat transfer and fluid friction (S_{total} ; Eq. (25)), and average Bejan number (Be_{av} ; Eq. (28)) versus Rayleigh number in various cases for Pr = 0.026 and 988.24 are presented in Figures. 14 and 15. Average Bejan number (Be_{av}) indicates the importance of entropy generation due to heat transfer or fluid friction irreversibilities. As mentioned earlier, $Be_{av} > 0.5$ indicates that entropy generation is heat transfer dominant while $Be_{av} < 0.5$ indicates fluid friction dominant entropy generation. Further, cup-mixing temperature (Θ_{cup}) and RMSD based on Eqs. (29) and (30) are evaluated in order to compare various cases for higher thermal mixing and large temperature uniformity.

The total entropy generation is found to increase with Ra in all cases for both the Pr. On the other hand, the average Bejan number decreases with Ra. At low Ra, higher S_{total} is observed in case 1, followed by cases 5, 4, 2 and 3, respectively irrespective of Pr. The corresponding Be_{av} values are nearly equal to 1, indicating that the heat transfer irreversibility dominates over frictional irreversibility. The lower values of frictional irreversibilities is due to weak fluid flow in the cavity at low Ra. The increase in S_{total} with Ra is due to an increase in frictional irreversibilities, which is illustrated by a decrease in Be_{av} . It is found that S_ψ completely dominates S_{total} at critical Ra which occurs at about Ra = $3-4 \times 10^4$ for Pr = 0.026 and at Ra = $2-3 \times 10^4$ for Pr = 988.24. However, the critical Ra for case 1 with Pr = 0.026 occurs at a higher value, Ra = 9×10^4 .

A comparison of various cases indicates that entropy generation during the convection dominant case at Ra = 10^5 is higher in case 5 for Pr = 0.026 and in the uniform heating case (case 1) for Pr = 988.24. The higher value of S_{total} in those cases is primarily due to increase in frictional irreversibility as indicated by a lower value of $Be_{av} < 0.5$. On the other hand, the minimum entropy generation occurs in case 3, where the bottom wall is hot and side walls are cooled linearly for both Pr. It is interesting to note that the Be_{av} is also less than 0.5 for case 3, indicating that the lower S_{total} is due to an insignificant rise in S_θ compared to S_ψ . It may be noted that the

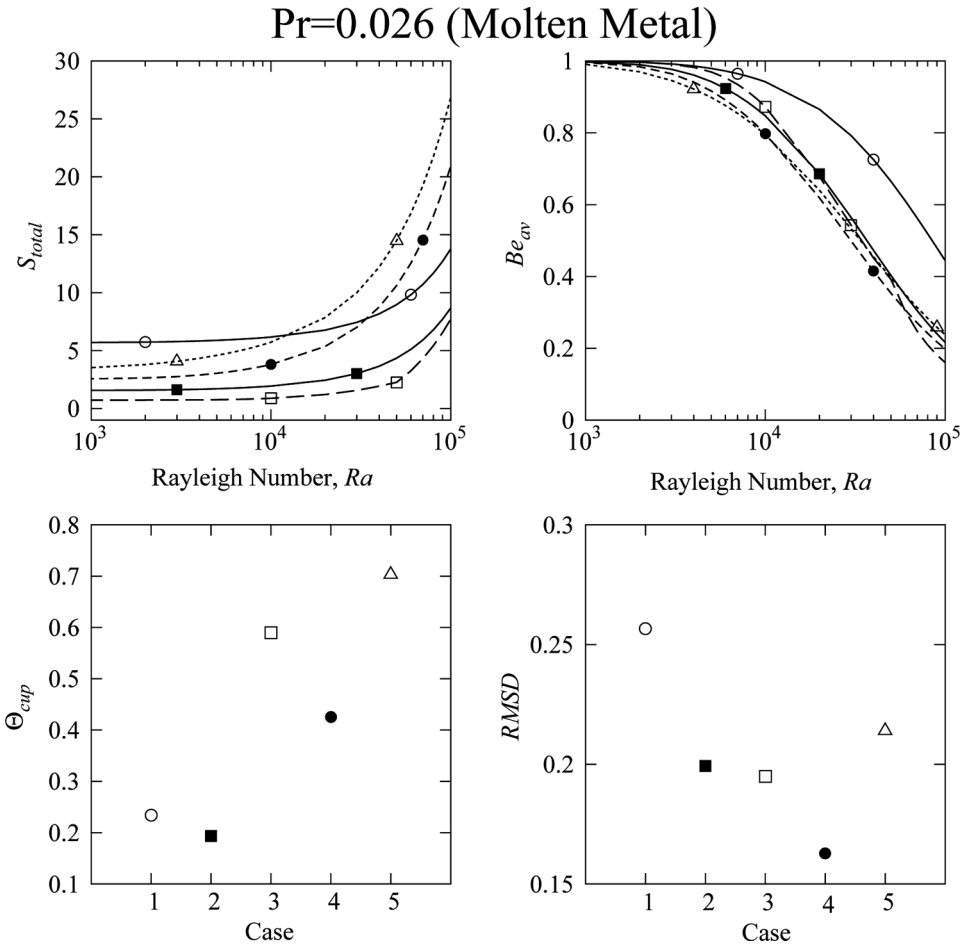


Figure 14. Upper panels: Variation of total entropy generation (S_{total}) and average Bejan number (Be_{av}) with Rayleigh number (Ra) for $Pr = 0.026$ (molten metal) with various thermal boundary conditions: case 1 (—○—), case 2 (—■—), case 3 (—□—), case 4 (—●—), and case 5 (⋯△⋯). Lower panels: Cup-mixing temperature (Θ_{cup}) and RMSD in various cases at $Ra = 10^5$.

dominance of frictional irreversibility is higher in case 3 compared to the other case as indicated by $Be_{av} = 0.16$ for $Pr = 0.026$ and 0.1 for $Pr = 988.24$, which are lower compared to that in all other cases.

Analysis of thermal mixing in various cases indicates that a higher Θ_{cup} for $Pr = 0.026$ is observed in case 5 ($\Theta_{cup} = 0.70$), followed by cases 3, 4, 1 and 2, respectively (see lower panels of Figure 14). Corresponding RMSD values indicate that a higher degree of temperature uniformity is observed in case 4, followed by 3, 2, 5, and 1, respectively. It is interesting to observe cup-mixing temperature and degree of temperature uniformity for cases 1 and 2. The Θ_{cup} values for both cases differ only by a small value, but a higher degree of temperature uniformity is observed with sinusoidal heating in case 2 compared to case 1. This result clearly depicts

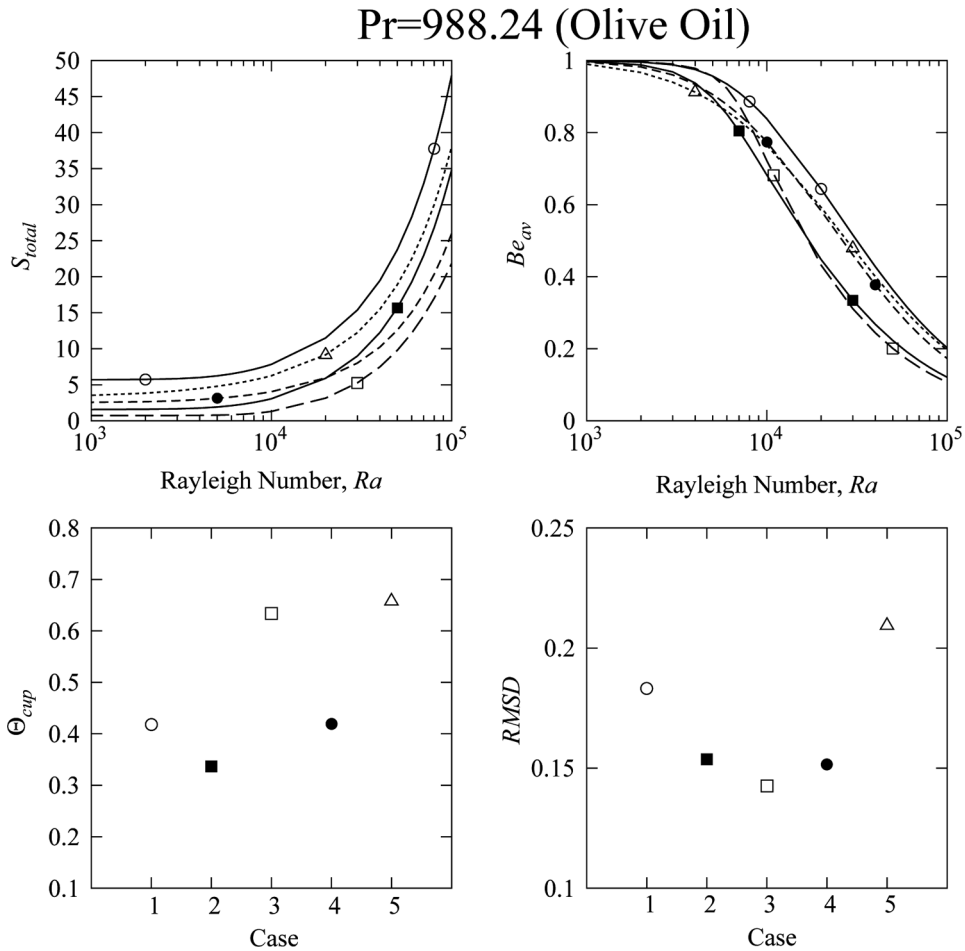


Figure 15. Upper panels: Variation of total entropy generation (S_{total}) and average Bejan number (Be_{av}) with Rayleigh number (Ra) for $Pr = 988.24$ (olive oil) with various thermal boundary conditions: case 1 (—○—), case 2 (—■—), case 3 (—□—), case 4 (—●—), and case 5 (⋯△⋯). Lower panels: Cup-mixing temperature (Θ_{cup}) and RMSD in various cases at $Ra = 10^5$.

the importance of thermal boundary conditions on overall thermal mixing and temperature uniformity in the cavity.

Case 5 is also found to result in the highest Θ_{cup} for $Pr (=988.24)$ with a value of 0.66 (see lower panels of Figure 15). The thermal mixing in case 3 is found to be slightly less compared to that in case 5, with $\Theta_{cup} = 0.63$. It may be noted that the Θ_{cup} is nearly equal in cases 1 and 4. It is interesting to observe that a temperature non-uniformity is higher in case 5 as seen from RMSD value, although the Θ_{cup} value is high. In contrast, a higher Θ_{cup} and lower RMSD value is observed for case 3, indicating that the fluid is well-mixed in the cavity, and a large region of the cavity is maintained at the highest possible temperature. The nonuniformity in temperature

distribution is higher in case 1 compared to that in case 4 (see RMSD values), although Θ_{cup} is nearly equal in both cases.

Overall, it may be noted that total entropy generation (S_{total}) in case 3 for $\text{Pr} = 0.026$ is low, in addition to higher thermal mixing and temperature uniformity. Note, that cases 4 and 5 result in high total entropy generation in the convection-dominant regime, although a highest Θ_{cup} is observed in case 5 and lower RMSD is observed in case 4. The efficacy of case 3 for $\text{Pr} = 988.24$ is clearly evident from higher Θ_{cup} , low RMSD and smallest S_{total} . Based on the above analysis, it may be concluded that case 3 configuration is suitable for efficient processing of materials for all limits of Pr .

4. CONCLUSION

The present study deals with entropy generation during natural convection in a square cavity subjected to various thermal boundary conditions. The local entropy generation due to heat transfer and fluid friction irreversibilities are analyzed via local entropy maps for fluid with $\text{Pr} = 0.026$ (molten metals) and 988.24 (olive oil) within a range of Rayleigh numbers, $\text{Ra} = 10^3$ – 10^5 . The governing equations are solved by the Galerkin finite element method to predict flow and temperature distributions. The elemental basis set has been used to evaluate the entropy generation terms due to heat transfer (S_{θ}) and fluid friction (S_{ψ}). The derivatives at a node are calculated based on the function values of adjacent elements that share the node through elemental basis set, and this approach offers accurate estimation of S_{θ} and S_{ψ} . Detailed investigation on the effects of various thermal boundary conditions on S_{θ} and S_{ψ} is presented. The variation of total entropy generation and average Bejan number (Be_{av}) with respect to Ra are analyzed. Furthermore, the thermal mixing and the degree of temperature uniformity are evaluated based on cup-mixing temperature and root-mean square deviation (RMSD).

During the conduction-dominant regime at low Ra , it is found that the heat transfer irreversibility dominates the entropy generation in the cavity. The maximum entropy generation due to heat transfer occurs near the hot-cold junctions, where high thermal gradients occur. On the other hand, the entropy generation due to frictional irreversibility are lower as the fluid flow is weak at low Ra and thus the velocity gradients are lower resulting in low S_{ψ} . At higher Ra ($\text{Ra} = 10^5$), the fluid flow is intensified resulting in enhanced heat transfer. Consequently, the thermal as well as velocity gradients increase significantly. It is found that the frictional irreversibility competes with thermal irreversibility at higher Ra and S_{ψ} also dominates the entropy generation in all cases for all Pr . The local maps of entropy generation due to heat transfer (S_{θ}) and fluid friction (S_{ψ}) are observed to be qualitatively similar in case 1 and 2 (uniform and sinusoidal heating). Further, the maps of S_{ψ} are found to be similar in cases 4 and 5. The heat transfer and fluid friction irreversibilities are found to be higher for higher Pr fluid.

Comparison of all cases indicated that a minimum total entropy generation, highest cup-mixing temperature and higher degree of temperature uniformity occurs in case 3, where the bottom wall is hot and side walls are cooled linearly. The frictional irreversibility is found to dominate S_{total} in case 3, indicating that the heat transfer irreversibility is least in case 3 among all cases. It is concluded that case 3 type of configuration may be preferred for efficient processing of various fluids.

REFERENCES

1. I. E. Sarris, I. Lekakis, and N. S. Vlachos, Natural Convection in a 2-D Enclosure with Sinusoidal Upper Wall Temperature, *Numer. Heat Transfer A*, vol. 42, pp. 513–530, 2002.
2. I. E. Sarris, I. Lekakis, and N. S. Vlachos, Natural Convection in Rectangular Tanks Heated Locally from Below, *Int. J. Heat Mass Transfer*, vol. 47, pp. 3549–3563, 2004.
3. J. Ma, P. Guo, J. Zhang, N. Li, and B. M. Fu, Enhancement of Oxygen Transfer in Liquid Lead and Lead-Bismuth Eutectic by Natural Convection, *Int. J. Heat Mass Transfer*, vol. 48, pp. 2601–2612, 2005.
4. N. B. Cheikh, B. B. Beya, and T. Lili, Influence of Thermal Boundary Conditions on Natural Convection in a Square Enclosure Partially Heated from Below, *Int. Comm. Heat Mass Transfer*, vol. 34, pp. 369–379, 2007.
5. E. Bilgen and R. B. Yeddera, Natural Convection in Enclosure with Heating and Cooling by Sinusoidal Temperature Profiles on One Side, *Int. J. Heat Mass Transfer*, vol. 50, pp. 139–150, 2007.
6. H. Asan and L. Namli, Laminar Natural Convection in a Pitched Roof of Triangular Cross-Section: Summer Day Boundary Conditions, *Energy Buildings*, vol. 33, pp. 69–73, 2000.
7. T. Basak, S. Roy, and A. R. Balakrishnan, Effects of Thermal Boundary Conditions on Natural Convection Flows within a Square Cavity, *Int. J. Heat Mass Transfer*, vol. 49, pp. 4525–4535, 2009.
8. M. Corcione, Effects of the Thermal Boundary Conditions at the Sidewalls upon Natural Convection in Rectangular Enclosures Heated from Below and Cooled from Above, *Int. J. Thermal Sciences*, vol. 42, pp. 199–208, 2003.
9. S. C. Saha, J. C. Patterson, and C. Lei, Scaling of Natural Convection of an Inclined Flat Plate: Ramp Cooling Condition, *Int. J. Heat Mass Transfer*, vol. 53, pp. 5156–5166, 2010.
10. T. Fusegi, J. M. Hyun, and K. Kuwahara, A Numerical Study of 3-D Natural Convection in a Cube: Effects of the Horizontal Thermal Boundary Conditions, *Flu. Dyn. Res.*, vol. 8, pp. 221–230, 1991.
11. Q. W. Wang, J. Yang, M. Zeng, and G. Wang, Three-Dimensional Numerical Study of Natural Convection in an Inclined Porous Cavity with Time Sinusoidal Oscillating Boundary Conditions, *Int. J. Heat Fluid Flow*, vol. 31, pp. 70–82, 2010.
12. H. Wang and M. S. Hamed, Flow Mode-Transition of Natural Convection in Inclined Rectangular Enclosures Subjected to Bidirectional Temperature Gradients, *Int. J. Thermal Sciences*, vol. 45, pp. 782–795, 2006.
13. D. E. Ameziani, R. Bennacer, K. Bouhadeif, and A. Azzi, Effect of the Days Scrolling on the Natural Convection in an Open Ended Storage Silo, *Int. J. Thermal Sciences*, vol. 48, pp. 2255–2263, 2009.
14. T. P. Bednarz, C. Lei, and J. C. Patterson, Unsteady Natural Convection Induced by Diurnal Temperature Changes in a Reservoir with Slowly Varying Bottom Topography, *Int. J. Thermal Sciences*, vol. 48, pp. 1932–1942, 2009.
15. A. Bejan, *Entropy Generation Minimization*, CRC Press, Boca Raton, 1982.
16. M. Magherbi, H. Abbasi, and A. Ben Brahim, Entropy Generation at the Onset of Natural Convection, *Int. J. Heat Mass Transfer*, vol. 46, pp. 3441–3450, 2003.
17. G. G. Illis, M. Mobedi, and B. Sunden, Effect of Aspect Ratio on Entropy Generation in a Rectangular Cavity with Differentially Heated Vertical Walls, *Int. Comm. Heat Mass Transfer*, vol. 35, pp. 696–703, 2008.
18. A. C. Baytas, Entropy Generation for Natural Convection in an Inclined Porous Cavity, *Int. J. Heat Mass Transfer*, vol. 43, pp. 2089–2099, 2000.

19. W. J. Yang, T. Furukawa, and S. Torii, Optimal Package Design of Stacks of Convection-Cooled Printed Circuit Boards using Entropy Generation Minimization Method, *Int. J. Heat Mass Transfer*, vol. 51, pp. 4038–4046, 2008.
20. I. Dagtekin, H. Oztop, and A. Bahloul, Entropy Generation for Natural Convection in Γ -Shaped Enclosures, *Int. Comm. Heat Mass Transfer*, vol. 34, pp. 502–510, 2007.
21. Y. Varol, H. Oztop, and A. Koca, Entropy Generation due to Conjugate Natural Convection in Enclosures Bounded by Vertical Solid Walls with Different Thickness, *Int. Comm. Heat Mass Transfer*, vol. 35, pp. 648–656, 2008.
22. I. Zahmatkesh, On the Importance of Thermal Boundary Conditions in Heat Transfer and Entropy Generation for Natural Convection Inside a Porous Enclosure, *Int. J. Thermal Sciences*, vol. 47, pp. 339–346, 2008.
23. D. R. Kassoy and A. Zebib, Convection Fluid Dynamics in a Model of a Fault Zone in the Earth's Crust, *J. Fluid Mech.*, vol. 88, pp. 789–792, 1978.
24. A. K. Singh, R. Pardeshi, and B. Basu, Modelling of Convection during Solidification of Metal and Alloys, *Sadhana*, vol. 26, pp. 139–162, 2001.
25. J. N. Reddy, *An Introduction to the Finite Element Method*, McGraw-Hill, New York, 1993.
26. M. M. Ganzarolli and L. F. Milanez, Natural Convection in Rectangular Enclosures Heated from Below and Symmetrically Cooled from the Sides, *Int. J. Heat Mass Transfer*, vol. 38, pp. 1063–1073, 1995.